Numerical Investigation of Propeller–Flap Interaction in Inclined Over-the-Wing Distributed-Propulsion Systems

Bölk, S.A.; de Vries, R.; van Arnhem, N.; Veldhuis, L.L.M.

DOI
10.2514/6.2021-0603

Publication date
2021

Document Version
Final published version

Published in
AIAA Scitech 2021 Forum

AIAA SciTech Forum
11–15 & 19–21 January 2021, VIRTUAL EVENT
AIAA Scitech 2021 Forum

10.2514/6.2021-0603

Numerical Investigation of Propeller–Flap Interaction in Inclined Over-the-Wing Distributed-Propulsion Systems

Sören Bölk*, Reynard de Vries †, Nando van Arnhem ‡, and Leo L. M. Veldhuis §
Delft University of Technology, Delft, 2629 HS, The Netherlands

In this study, unsteady RANS simulations are performed to investigate the effect of over-the-wing (OTW) propeller inclination on the aerodynamic interaction with a wing featuring a plain flap. A comparison to experimental data shows that the numerical approach is capable of modeling the wing and propeller separately and can capture the effect of the wing on the propeller in the OTW configuration, but under-predicts propeller-induced flow separation over the flap. The results show that, if the propeller is installed over the flap hinge and aligned with the freestream velocity (baseline configuration), the slipstream and blade tip-vortices generate additional adverse pressure gradients on the wing surface, leading to a local increase in flow separation downstream. However, if the propeller is tilted and aligned with the flap surface (inclined configuration), the slipstream increases the momentum in the boundary layer and the flow remains attached. The propeller alters the pressure distribution of the wing such that higher lift is generated in the baseline case, while a larger drag reduction is achieved in the inclined case. However, combined with the thrust vector of the propeller, the baseline configuration is found to have the largest combined axial force in thrust direction, while the inclined configuration presents the highest effective lift. These results indicate that inclining the propeller can enhance the low-speed performance of OTW distributed-propulsion systems.

Nomenclature

b	=	wingspan [m]	L	=	lift [N]
c	=	chord [m]	n	=	angular velocity [Hz]
c_d	=	sectional drag coefficient $d/(q_\infty c)$ [-]	N	=	normal force [N]
C_D	=	drag coefficient $D/(q_\infty cb)$ [-]	p	=	observed order of grid convergence [-] or pressure [Pa]
c_l	=	sectional lift coefficient $l/(q_\infty c)$ [-]			
C_L	=	lift coefficient $L/(q_\infty cb)$ [-]	P_s	=	shaft power [W]
C_p	=	pressure coefficient $(p-p_\infty)/q_\infty$ [-]	q_∞	=	free-stream dynamic pressure $0.5\rho_\infty V_\infty^2$ [Pa]
C_P	=	power coefficient $P_\mathrm{s}/(\rho_\infty n^3 D_\mathrm{p}^5)$ [-]	Q	=	torque [Nm]
C_Q	=	torque coefficient $Q/(\rho_\infty n^2 D_\mathrm{p}^5)$ [-]	r	=	radial coordinate [m]
C_T	=	thrust coefficient $T/(\rho_\infty n^2 D_\mathrm{p}^4)$ [-]	R	=	propeller radius [m] or resultant force [N]
C_T'	=	thrust coefficient distribution $dC_T/d(r/R)$ [-]			
C_ω	=	vorticity coefficient $\omega/(2\Omega)$ [-]	Re	=	Wing-chord-based Reynolds number [-]
d	=	sectional drag [N/m] or distance from wall [m]	T	=	thrust [N]
			$\hat{T}_c$	=	thrust coefficient $T/(S_\mathrm{ref} q_\infty)$ [-]
D	=	drag [N]	S_ref	=	reference area $1.1cD_\mathrm{p}$ [m^2]
D_p	=	propeller diameter [m]	U, V, W	=	velocities in baseline coordinate system [m/s]
F	=	force [N]	u, v, w	=	velocities in inclined coordinate system [m/s]
J	=	advance ratio $V/(nD)$ [-]	U_ξ	=	discretization uncertainty of a quantity ξ [-]
k	=	turbulent kinetic energy [m^2/s^2]	U_∞	=	free-stream velocity [m/s]
l	=	sectional lift [N/m]	x, y, z	=	Cartesian coordinates [m]

*MSc Student, Flight Performance and Propulsion Section, Faculty of Aerospace Engineering, soeren.boelk@gmail.com, AIAA Member.
†PhD Candidate, Flight Performance and Propulsion Section, Faculty of Aerospace Engineering, R.deVries@tudelft.nl, AIAA Member.
‡PhD Candidate, Flight Performance and Propulsion Section, Faculty of Aerospace Engineering, N.vanArnhem@tudelft.nl, AIAA Member.
§Full Professor, Flight Performance and Propulsion Section, Faculty of Aerospace Engineering, AIAA Member.

y^+ = non-dimensional wall-distance [-]
δ_{99} = boundary-layer thickness [m]
δ_f = flap deflection angle [deg]
$\Delta(\ )$ = difference between numerical and experimental or propeller-on and propeller-off
Δ_ξ = data range parameter [-]
ε = tip clearance [m]
ϵ = discretization error [-]
σ = standard deviation [-]
ϕ = phase angle [deg]
ω = vorticity [s^{-1}] or specific dissipation rate [s^{-1}]
Ω = angular velocity [rad/s]

I. Introduction

Worldwide air travel is predicted to increase by 4.7% per year between the years 2008 and 2025 [1]. Due to this increasing demand for air travel, and consequently jet fuel, new solutions need to be found to limit the ecological impact of aviation while serving the demand for air travel by a population growing in size and wealth. With this in mind, the National Aeronautics and Space Administration (NASA) [2] and the European Commission [3] defined goals targeting emissions, noise, fuel burn, and take-off field length. In order to meet these challenging requirements, new aircraft designs and new propulsion sources, such as Hybrid-Electric Propulsion (HEP) [4], are investigated, which in turn enable advantageous propulsion-integration concepts like Distributed Propulsion (DP) [5, 6]. In these configurations, the aerodynamic interaction effects between the propulsive devices and the airframe are exploited to reduce the fuel consumption, emissions, noise, and take-off and landing distance of the aircraft [6–9].

An example of such propulsion-system configurations is the over-the-wing (OTW) distributed-propulsion concept [10, 11]. Previous studies have shown that mounting a propeller above a wing can increase the lift-to-drag ratio of the wing by increasing lift and reducing pressure drag [12, 13] in both high-lift [14] and cruise [15] conditions. Moreover, compared to tractor propellers, OTW propellers overcome ground clearance limitations and have the potential to emit less noise to the ground due to shielding by the wing [16]. Although OTW propellers have been studied in channel-wing configurations since the early 1950s [17, 18], the recent developments in the field of distributed propulsion have led to an increased interest in ducted OTW systems with reduced propeller diameter and an increased number of propulsors [19–22]. In these configurations, the array of propulsors can be installed near the trailing edge and deflected with the flap, further enhancing high-lift capabilities by means of thrust vectoring [10, 11, 19].

However, both numerical [23] and experimental [24] studies have shown that, in OTW systems, the interaction between the propeller and the wing boundary-layer can lead to flow separation over the flap in high-lift conditions. This detrimental effect cannot be accurately captured with steady RANS simulations [23] and is particularly important to consider at low advance ratios and high-thrust settings [24], i.e., in take-off conditions. Moreover, it is unclear how well unsteady simulations capture this effect, and whether the flow separation is effectively mitigated when the propeller is inclined with the flap. Given the decisive impact of the system's high-lift capabilities on the design of distributed-propulsion aircraft [25], a fundamental understanding of the problem and how to model it is required before detailed conclusions can be drawn regarding the overall performance of OTW DP systems.

The goal of this study is therefore to investigate the aerodynamic interaction between an inclined OTW propeller and the wing flap using unsteady CFD analyses. A single, unducted propeller is simulated, to isolate the interaction effects from additional interactions with ducts or adjacent propellers. Given the challenges associated to numerically predicting flow separation in the presence of highly localized, unsteady, three-dimensional pressure gradients, a simplified wing geometry with available validation data is used. The propeller and wing geometry are described along with the computational setup in Sec. II. A step-by-step approach is then taken to identify the aerodynamic interaction phenomena that affect flow separation. First, the simulations are performed with wind-tunnel walls and compared to experimental data in the verification & validation section (Sec. III). The aerodynamic interaction phenomena are subsequently described in Sec. IV for both baseline and inclined propeller configurations. Finally, Sec. V discusses how the interaction effects influence the loading distributions on the propeller and wing, and how these are in turn related to system performance.

II. Computational Setup

In the following sections, the computational set up will be explained, starting with the geometry of the wing and propeller models (Sec. II.A). Then, the solver setup will be discussed in Sec. II.C. Subsequently, Sec. II.B presents the computational domain and operating conditions. Finally, the propeller modeling technique is described in Section II.D.

A. Geometry and Operating Conditions

For validation purposes, the wing and propeller geometry of the experimental study described in Ref. [24] is used. The wing has a chord of $c = 1.042$ m and features a flat upper surface, on which a pressure gradient can be generated by deflecting a plain flap of 20% chord. The main dimensions of the wing profile and propeller are given in Fig. 1. Details of the geometry can be found in Ref. [24].

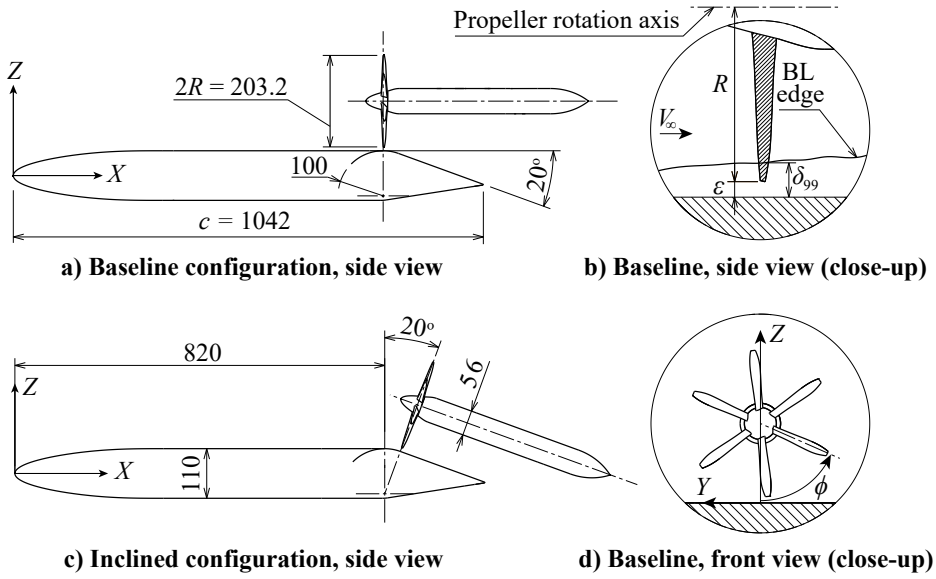

a) Baseline configuration, side view **b) Baseline, side view (close-up)**

c) Inclined configuration, side view **d) Baseline, front view (close-up)**

Fig. 1 Wing and propeller geometry. The dimensions are in mm.

The propeller is positioned above the flap hinge at $x/c = 0.79$. This location is chosen based on previous studies, which show that mounting the propeller close to the trailing edge represents a good compromise between lift gain, drag reduction, and propulsive efficiency loss [19]. The propeller features six blades with a diameter of 0.2032 m ($D_p/c = 0.2$) and a blade pitch of 45° at 70% of the blade radius. The detailed geometry of a propeller blade, including the chord and blade pitch-angle distribution, can be found in Ref. [26].

The inclined OTW propeller position is derived from the baseline configuration by rotating the propeller around the flap hinge by the flap-deflection angle, $\delta_f = 20°$, as shown in Fig. 1c. Consequently, the inclined propeller is positioned behind the flap curvature, closer to the trailing edge than the baseline propeller, and the axis of the inclined propeller is parallel to the suction side of the flap. This configuration would be obtained if the propeller were physically attached to the flap mechanism. The gap between the propeller tips and the wing surface, ε, is 7.5 mm ($\varepsilon/R = 0.0738$) in both configurations. This corresponds to approximately 50% of the boundary-layer thickness that would be obtained without propeller or flap deflection at the baseline propeller location, as determined in Ref. [24]. The definition of the boundary-layer thickness, δ_{99}, is based on the total pressure that is associated with 99% free-stream velocity.

The simulations are performed at a free-stream velocity of $U_\infty = 20$ m/s, since validation data is available for this velocity magnitude. This corresponds to a Reynolds number based on the wing-chord of $Re = 1.4 \cdot 10^6$. A flap deflection angle of 20 degrees is selected, at which preliminary simulations of the isolated wing show that the flow stays attached over the curvature of the flap on the suction side but starts to separate at $x/c = 0.86$. The rotational speed of the propeller is kept constant at n = 87 Hz, which corresponds to an advance ratio of $J = 1.13$. At this advance ratio, the propeller is operating at high thrust in uninstalled conditions ($C_T = 0.35$), being representative of a typical take-off thrust setting.

B. Computational Domain

The computational domain of the isolated propeller simulations is shown in Fig. 2a. Throughout this paper, the working fluid is air and is treated as a compressible, ideal, gas, where Sutherland's Law is used to calculate the dynamic viscosity. The walls of the propeller blade, spinner, and nacelle are modeled as no-slip walls with a first layer height below $y^+ = 1$. The total gauge pressure and total temperature are specified at the inlet whereas, at the outlet, the pressure is prescribed to be the ambient, standard, sea-level pressure. Values for the turbulence quantities k and ω are chosen

based on the recommendations by Spalart and Rumsey [27], and source terms are used in the flow to prevent their decay from the inlet to the model. Only one blade with periodic boundary conditions is modeled in the domain to reduce the required calculation time. At the top boundary, a pressure far-field condition is used with a prescribed Mach number, static pressure, and static temperature corresponding with the inlet condition. The mesh is locally refined in areas close to the propeller geometry, as well as upstream and downstream of the propeller, as shown in Fig. 2b.

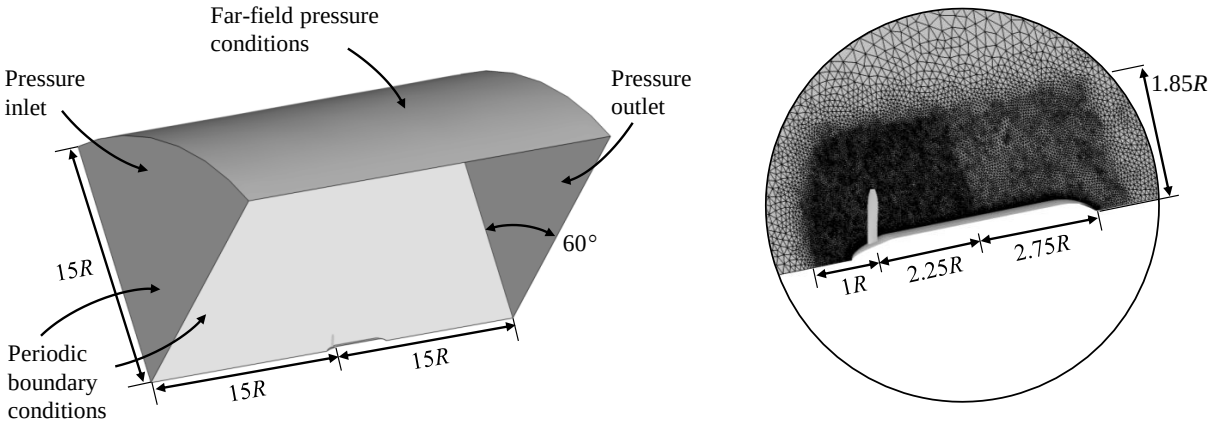

(a) Boundary conditions of the computational domain.

(b) Close-up view of the refined grid around the propeller geometry.

Fig. 2 Computational domain of the isolated propeller.

The dimensions of the isolated wing and its domain are identical to the ones of the installed OTW simulations, except for the volume where the propeller mesh is added with the overset technique. Therefore, only the domain of the OTW configuration is shown in Fig. 3. The comparison of the numerical to the experimental results is done for the baseline configuration with wind tunnel walls, shown in Figs. 3a and 3b, where the cross-section in Fig. 3a has the same dimensions as the test-section used in Ref. [24]. The domain extends approximately three chords upstream and

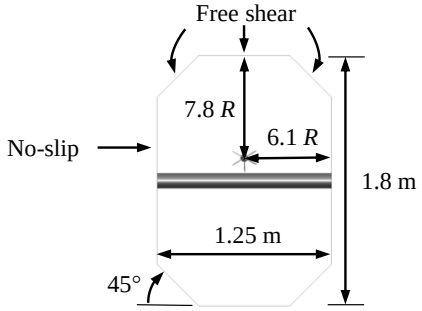

(a) Front view (with walls)

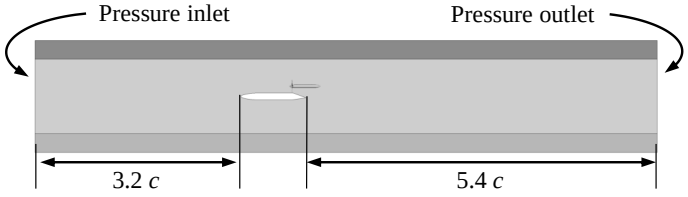

(b) Side view (with walls)

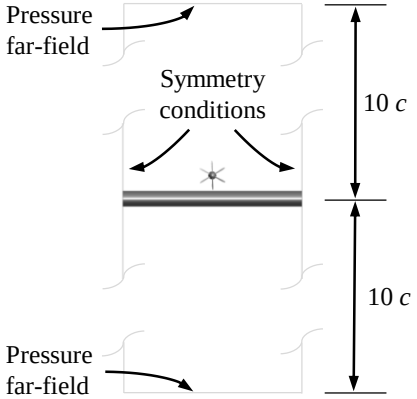

(c) Front view (without walls)

Fig. 3 Computational domain of the configurations with wind tunnel walls, (a) and (b), as well as without (c).

five chords downstream of the wing. For the comparison to experimental data (Sec. III.C), the sidewalls of the wind tunnel that intersect with the wing model are modeled as a no-slip boundary condition to account for the interaction of the wing with the wind-tunnel boundary-layer. To reduce the computational effort, however, a wall-function approach is used at these sidewalls, contrary to the resolved boundary-layer with $y^+ < 1$ on the wing. All other walls of the wind tunnel are set as free-slip walls. In the remaining studies (Secs. IV and V), the influence of the wind tunnel walls is removed by changing the sidewalls to symmetry boundary conditions and extending the top and bottom of the domain with far-field pressure boundary conditions ten chord lengths away, as shown in Fig. 3c. The length and width of the domain is not changed, and all other solver settings are kept constant, compared to the domain with wind tunnel walls.

C. Solver Setup

The simulations are performed as unsteady, compressible, Reynolds-Averaged Navier–Stokes (RANS) calculations with the commercial, cell-centered, finite volume ANSYS Fluent 19.1 solver. Unsteady RANS simulations are chosen based on the findings in Ref. [23] and to avoid computational costs of, for instance, LES or DES that are not always justified [28–30]. To improve the accuracy of predicting flows with a strong adverse pressure gradient, the k-ω based Explicit Algebraic Reynolds Stress Model (EARSM) by Wallin and Johansson [31] is used to model turbulence. Reference [31] claims that the proposed model is numerically robust and only negligibly increases the computational costs compared to two-equation eddy viscosity models by explicitly relating the Reynolds Stresses to the mean flow field. At the same time, the model is supposed to predict effects of rotation, and the separation behavior of boundary-layers in adverse pressure gradients, better than two-equation models due to a more realistic representation of the anisotropy in the flow. The pressure and momentum coupling algorithm by Rhie-Chow [32] is used, where spatial discretization is achieved by second-order upwind schemes and a first-order implicit transient formulation is employed.

The unsteady calculations of the installed configurations are performed with a time-step that is equal to two degrees of propeller rotation, with 30 inner iterations. The isolated wing and propeller simulations, however, are performed as steady simulations with a Courant-Friedrichs-Lewy (CFL) condition of CFL = 2. A moving reference-frame approach is used for the isolated propeller calculation, where only one blade is simulated using periodic boundary conditions. A preliminary investigation, not shown here, confirmed that the steady-state approach did not appreciably affect the wing lift or propeller thrust in isolated conditions compared to the unsteady simulations of these isolated conditions.

D. Overset Grid

In OTW systems, the propeller and wing operate in close proximity. Since the boundary layer needs to be modeled on both components for both the baseline and the inclined configuration, a sliding mesh approach was considered unfeasible because of the strict requirement of an exact match in mesh size, which would result in an excessive number of cells. Instead, an overset approach was selected for two reasons: firstly, to reduce the number of cells required and, secondly, to be able to simulate the two configurations without having to completely redefine the mesh. In general, an overset grid consists of a background grid and at least one component grid that is inserted into the background with an overlap. In the overlapping area, the solution is either obtained by calculating it or interpolating the results from other overlapping, solved, cells. Due to the interpolation at the boundaries of the component meshes, conservation is not easily enforced [33]. Therefore, it is important that the overlapping cells of the background mesh and the component meshes have a similar size and the zones overlap sufficiently [34].

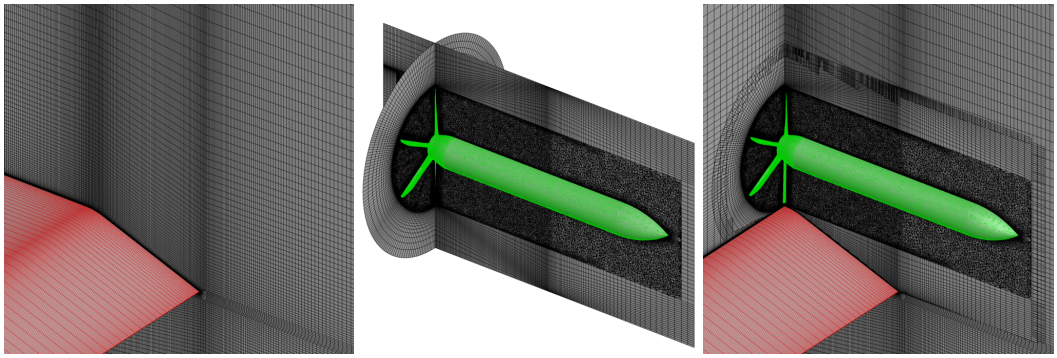

(a) Wing **(b) Propeller** **(c) Wing + propeller**

Fig. 4 Overset mesh assembly of the baseline configuration.

The overset mesh used in this paper features a structured wing mesh that serves as the background (Fig. 4a) and a separate propeller mesh (Fig. 4b) that is inserted into the background mesh. On the inside, the propeller mesh is the same unstructured mesh as in Fig. 2b for consistency. Towards the outside of the mesh, however, a structured grid is used for a sufficient overlap and transition to the structured wing mesh. The resulting OTW configuration is depicted in Fig. 4c. The overlap is minimized on cells of similar volume where the propeller mesh has a higher grid priority to enforce a constant position of the overset interface when the propeller rotates. Throughout the simulation, the wing mesh remains fixed while the propeller mesh rotates. Hence, in each time step, the connectivity between the two grids is re-established.

III. Uncertainty Quantification and Validation

This section discusses the numerical uncertainty due to the discretization error and presents the model errors by evaluating the influence of the overset interface and by comparing the numerical results to experimental ones. First, a grid convergence study of the isolated 2D wing and 3D propeller is performed in Sec. III.A to quantify the discretization error. Then, the influence of the overset interface is analyzed in Sec. III.B by performing simulations with an overset mesh excluding the propeller. Finally, Sec. III.C compares the numerical results of the isolated wing and propeller, as well as the baseline OTW configuration to experimental results.

A. Grid convergence study

The convergence history of the steady simulations of the wing geometry was such that the residuals dropped at least five orders of magnitude and the change in lift and drag over the last 100 iterations was less than 0.001%. Analogously, the isolated propeller simulations were run until the iterative error of the thrust and torque coefficients over the last 100 iterations was less than 0.001% and the residuals dropped at least five orders of magnitude. Therefore, the iterative error is relatively small, when compared to the discretization error. The discretization errors for the wing and propeller were estimated with four systematically refined grids by using a grid refinement ratio of 1.3. For each of the meshes, the first-layer height and number of layers in inflation layers were kept constant. The grids are denoted h_1 to h_4, where h_1 is the finest one, as shown in Table 1. The wing and propeller are considered separately, to save computing time and to ensure that the forces of the individual components are captured accurately, before combining them.

The discretization error is determined by using the procedure by Eça and Hoekstra [35]. The discretization error ϵ, is calculated by a power series expansion as $\epsilon = \alpha h_i^p$ where α is a constant to be determined, h_i is the representative grid cell size, and p is the observed order of grid convergence. The lift and drag values appear to diverge as the grid is refined, as shown in Figs. 5a and 5b. However, the resulting fits with the observed order converges towards finer grids and results in a low standard deviation σ, as shown in Table 2 for grid 3. Moreover, the observed order of convergence is very close to the theoretical order of two for both lift and drag. Although the observed order of convergence for drag is larger than two, it is within the range $0.5 \leq p < 2.1$. Therefore, it is considered as acceptable for monotonic convergence. The uncertainty in the numerical results indicated by the errorbars in Figures 5a and 5b is then estimated for a general quantity ξ as:

$$U_\xi = \begin{cases} 1.25 \cdot \epsilon_\xi + \sigma + |\xi_i - \xi_{\text{fit}}|, & \text{for } \sigma < \Delta_\xi \\ 3\frac{\sigma}{\Delta_\xi}(\epsilon_\xi + \sigma + |\xi_i - \xi_{\text{fit}}|), & \text{for } \sigma \geq \Delta_\xi \end{cases} \tag{1}$$

where Δ_ξ is a data range parameter defined in Ref. [35]. The resulting uncertainty estimation has a confidence level of 95%. For grid 3, the relative discretization error and uncertainty in lift and drag from Table 2 are relatively large. However, this is due to the low absolute lift and drag coefficients of the airfoil used in this paper. Figures 5a and 5b show that the absolute values of all four grids are already very close to each other and the accuracy is only marginally improved with a finer mesh. Furthermore, Fig. 5c shows that the velocity profile at the propeller location deviates hardly between grid 3 and grid 1. Therefore, grid 3 is selected for the wing.

Figures 6a and 6b show that both the thrust and torque coefficients of the isolated propeller converged with an observed order in the acceptable range. The thrust distribution in Fig. 6c shows no clear trend with grid refinement. Figure 7a, however, shows that at a distance to the propeller tip equal to the tip clearance used in the OTW configuration, only grid 4 results in considerably weaker velocity fluctuations, caused by the blade tip vortices, compared to the finer grids. This is attributed to an inaccurate capture of flow gradients, close to the blade tip vortices, with the refinement level of grid 4. Moreover, the total pressure in the slipstream varies with mesh refinement only in the region of the blade tip vortex, as is shown by the radial total pressure distributions in Fig. 7b. Only above $r/R = 0.8$ differences in total pressure can be found in the form of a stronger total pressure gradient for the finer grids, due to reduced

numerical diffusion. Therefore, the propeller grid 3 is used to keep the number of cells acceptable. This corresponds to a discretization error and uncertainty of the thrust and drag coefficients of the order of 1%, as listed in Table 2.

Table 1 Grids of the refinement study.

Grid	Wing		Propeller	
	h_i/h_1	Cells	h_i/h_1	Cells
Grid 1	1	208,212	1	14,463,300
Grid 2	1.27	128,342	1.25	7,346,487
Grid 3	1.62	79,404	1.55	3,909,325
Grid 4	2.04	50,224	1.87	2,192,981

Table 2 Results of the mesh refinement study for grid 3.

Parameter	Wing		Propeller	
	c_l	c_d	C_T	C_Q
p	1.98	2.05	1.72	1.98
ϵ [%]	-2.4	4.2	0.9	-0.5
σ [%]	0.28	0.44	0.04	0.07
U_ξ [%]	4.0	6.1	1.1	0.8

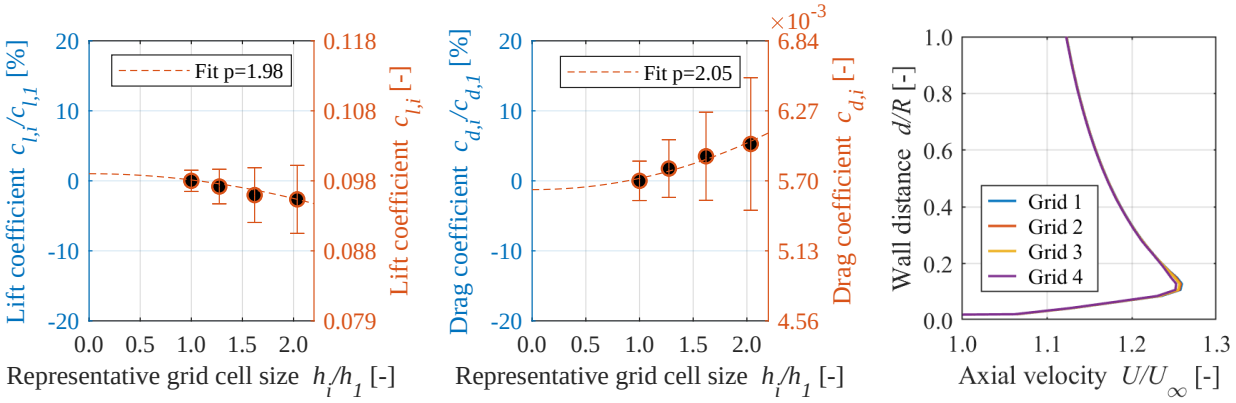

(a) Lift coefficient. **(b) Drag coefficient.** **(c) Inflow velocity.**

Fig. 5 Results of mesh refinement study of the two-dimensional wing section.

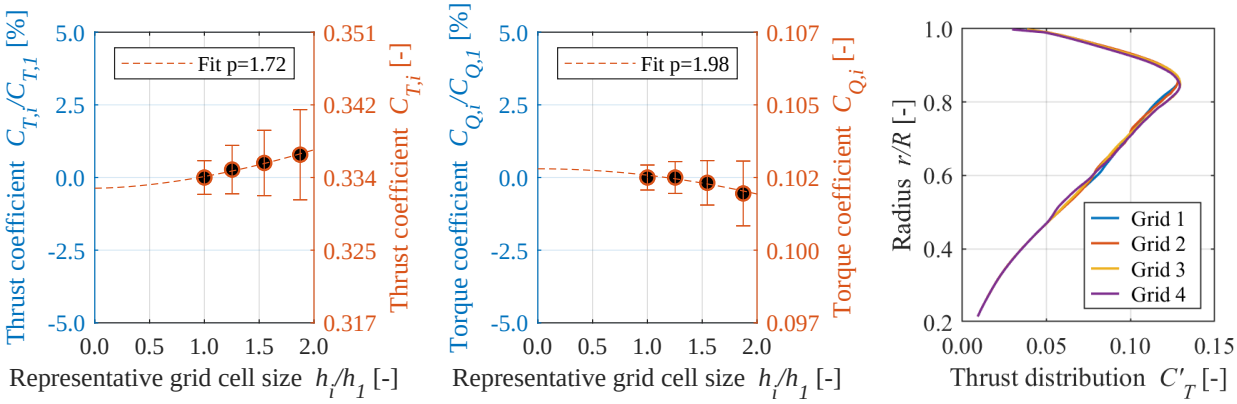

(a) Thrust coefficient. **(b) Torque coefficient.** **(c) Thrust distribution.**

Fig. 6 Mesh refinement study for the isolated propeller.

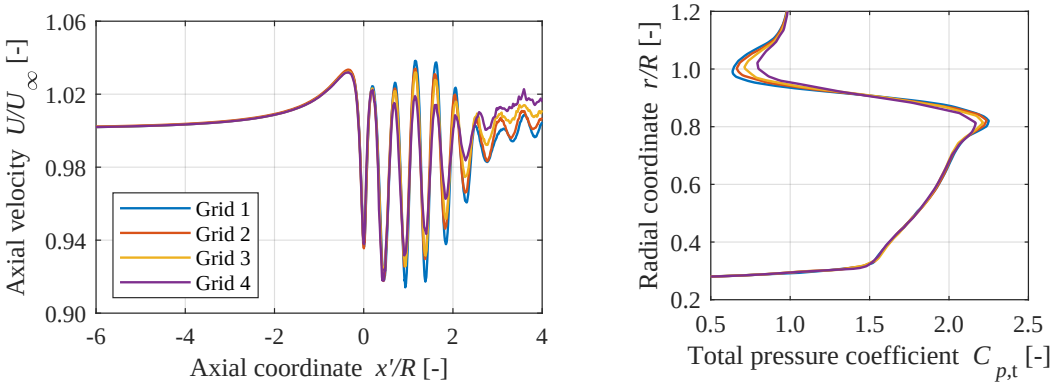

(a) Axial velocity profile. **(b) Total pressure distribution.**

Fig. 7 Axial velocity and total-pressure profiles in the isolated propeller slipstream, extracted from (a) an axial survey line ($r/R = 1.0738$) and (b) a radial survey line passing through the tip vortex ($x/R = 1$), respectively.

B. Influence of the overset interface

The overset interface is in close proximity with the wing's boundary-layer. The associated interpolation that is required between the stationary and rotating mesh may affect the boundary-layer profile, and therefore the interaction with the propeller tip. To determine the error of the overset implementation on the lift and drag of the wing, as well as on the boundary-layer at the propeller location, simulations were run with the wing and an "empty" overset mesh, i.e. excluding the propeller geometry. In this manner, the effect of the overset interface can be isolated by comparing the results to the ones of the wing without an overset mesh. The volumes of the overlapping cells are defined such that the overset interface is created approximately in the middle of the theoretical tip gap, following a cell-size based overlap minimization technique. The overset interface results in a local kink in the boundary-layer profile at a distance of approximately $d/c = 0.002$ to the wing-surface, as shown in Fig. 8a. At this location, the mesh of the wing and the propeller are merged and interpolation errors may arise in the flow gradients across the interface. Hence, close to the wing surface, the overset interface can cause an increase in wall shear due to an increased vertical velocity gradient. However, this has a negligible influence on the boundary-layer thickness δ_{99} indicated by the dots in Fig. 8a, which increases by less than 2%.

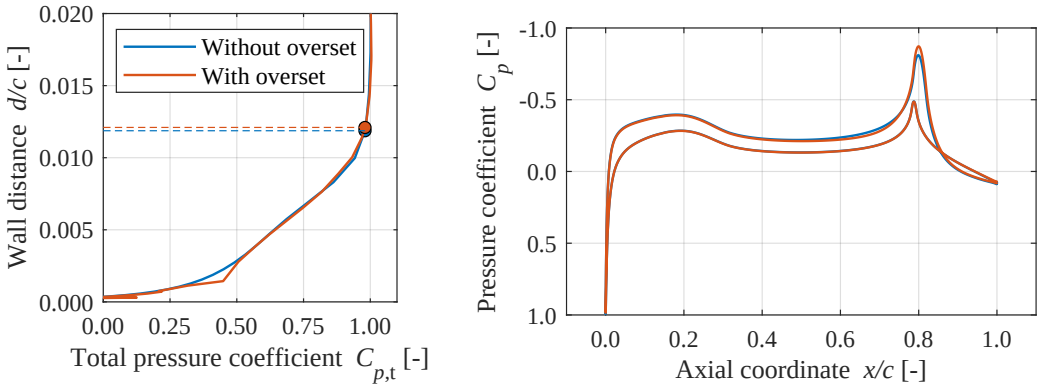

(a) Boundary-layer. profile **(b) Pressure distribution.**

Fig. 8 Influence of the overset interface on the boundary-layer profile and pressure distribution of the wing at the propeller location ($x/c = 0.79$).

The presence of the overset boundary also slightly affects the pressure distribution on the suction side of the wing, as shown in Fig. 8b. The overset boundary causes a more negative suction peak, leading to a small change in local lift of $\Delta C_l = +0.01$. The influence on drag coefficient, however, is even smaller, shown to be $\Delta C_d = +0.0001$. This is because

the increased velocity gradient at the wing surface leads to a slight delay in flow separation, such that the drag due to additional skin friction is compensated for by a reduction in pressure drag. It is therefore concluded that the influence on integral values are small. However, the observed irregularities in the boundary-layer profile should be taken into account when analyzing the interaction between the propeller and the wing's boundary-layer in the propeller-on configuration.

C. Comparison to experimental results

In order to gain further confidence in the numerical setup, the results of the isolated wing, propeller, and installed baseline configuration are compared with experimental results obtained in Refs. [24, 26]. In particular, the capability of the unsteady RANS simulations to capture propeller-induced flow separation on the flap will be assessed.

An important region for the propeller–wing interaction is the flowfield in the vicinity of the flap. Therefore, the measured flowfield at the flap (Fig 9a) is compared with the computed flowfield (Fig. 9b), for the propeller-off case. No significant difference between the experimental and numerical results can be found, indicating that the numerical approach is capable of predicting the flow field over the flap of the isolated wing with reasonable accuracy. This is confirmed by the comparison of the pressure distributions for the propeller-off case in Fig. 10a. The experimental results, however, exhibit a slightly lower axial velocity compared to the numerical results, despite a more downstream onset of flow separation, indicated by the contour-line of zero velocity in Fig. 9.

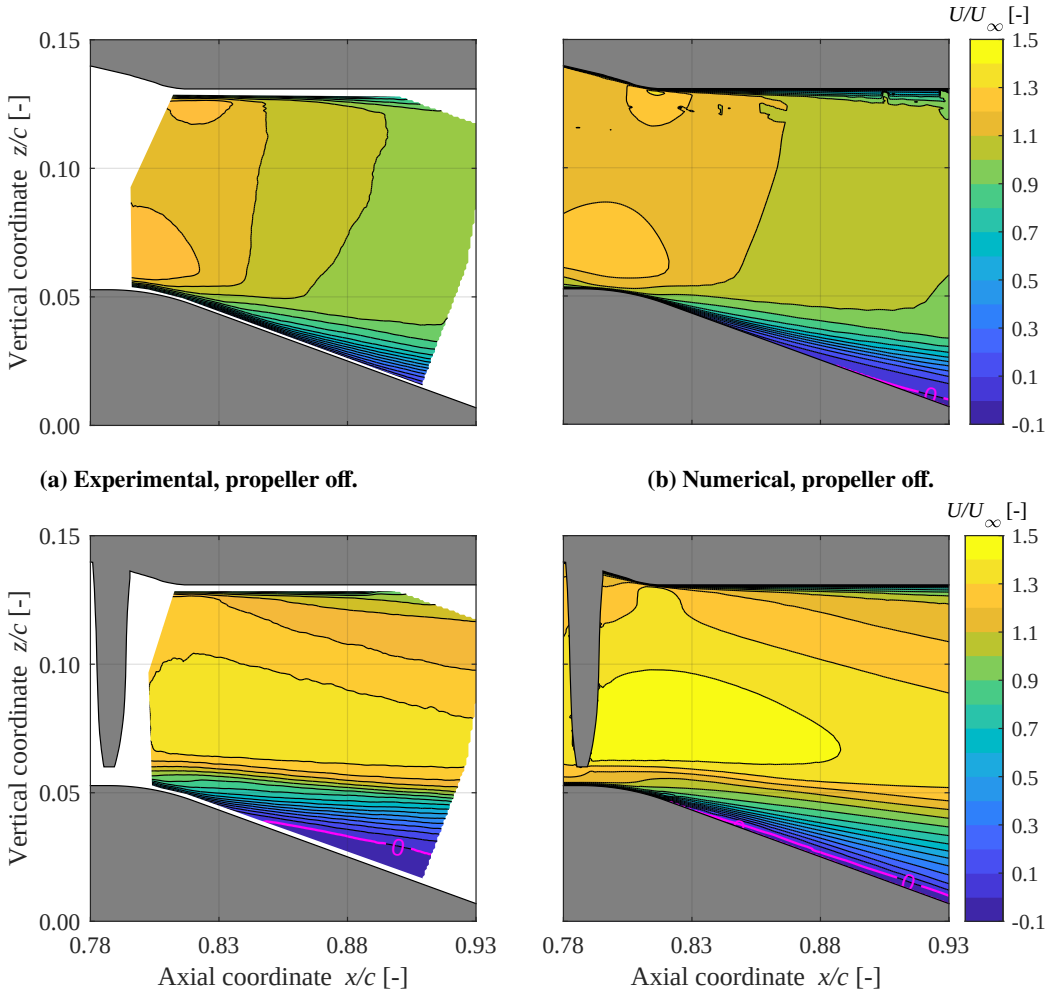

(a) Experimental, propeller off.

(b) Numerical, propeller off.

(c) Experimental, propeller on.

(d) Numerical, propeller on.

Fig. 9 Comparison between the time-averaged PIV measurement [24] and the time-averaged CFD RANS results for the axial velocity distribution over the flap.

Adding the propeller results in a stronger adverse pressure gradient at the propeller location that decreases the momentum in the boundary-layer over the flap and ultimately leads to earlier flow reversal than in the propeller-off case [24]. This effect of the propeller on flow separation, however, is more pronounced in the experimental results (Fig. 9c) than in the numerical ones (Fig. 9d). In the numerical results, the point of flow separation moves upstream when the propeller is included; however, the slipstream still deflects downwards and the flow remains more parallel to the flap surface than in the experiment. Consequently, the suction over the flap is stronger in the numerical results than in the experimental ones, as shown in Fig. 10b.

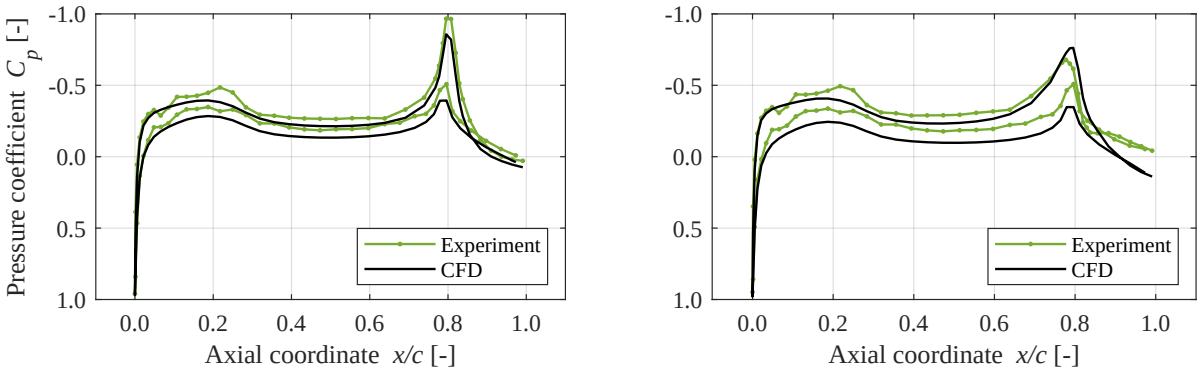

(a) Propeller off **(b) Propeller on**

Fig. 10 Comparison of wing pressure distributions obtained from the experimental and numerical results.

The differences in propeller-induced flow separation can be attributed to several factors. Firstly, all the turbulence in the flow is modeled, and not resolved—including the small turbulence scales close to the wing surface, where the flow reversal originates. Hence, the separation behavior is influenced by the selection of the turbulence model, and the ability of the model to predict flow separation can deteriorate when a propeller causes additional unsteady and highly-concentrated adverse pressure gradients. Secondly, numerical diffusion weakens the tip vortices, as shown in Fig. 11. This reduction in tip-vortex strength reduces the velocity deficits generated between the vortex core and the flap surface, therefore having a less detrimental effect on the boudary layer. Strong numerical diffusion can be found for

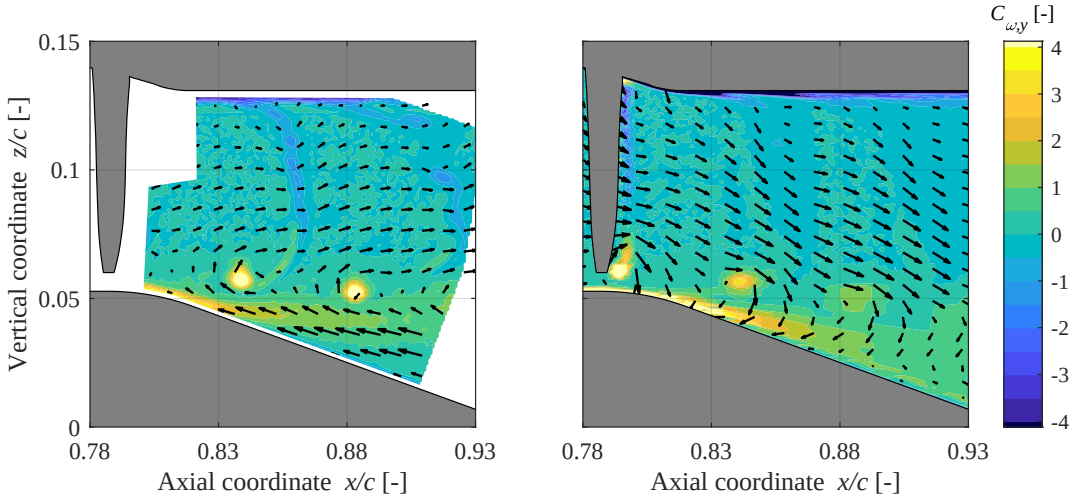

(a) Experimental **(b) Numerical**

Fig. 11 Comparison between the instantaneous CFD RANS results and the phase-locked PIV measurement for the out-of-plane vorticity over the flap, at the same phase angle ($\phi = 6°$). The vectors indicate the propeller-induced in-plane velocity.

various RANS turbulence models and is also indicative of an insufficient mesh resolution in the respective area [36]. Thirdly, the surface imperfections in the experiment, evident in Figs. 10a and 10b, may weaken the boundary-layer and increase the magnitude of flow separation. Finally, the overset mesh can lead to a small delay in flow separation, due to increased velocity gradients near the wing surface, as established in Section III.B. The overset interface may also further attenuate the influence of the blade tip vortices once the propeller is installed [37].

Tables 3 and 4 compare the resulting sectional pressure-lift and pressure-drag coefficients obtained below the propeller axis, as well as the propeller thrust coefficient. For the lift and drag coefficients,"uninstalled" refers to the propeller-off wing-configuration (i.e., with the nacelle present), whereas the uninstalled thrust coefficient is obtained from the isolated propeller. The thrust coefficients predicted by the CFD simulations show an acceptable agreement with the values obtained in the experiment, showing a difference of $\Delta C_T = -0.017$ (4.8%) and $\Delta C_T = -0.007$ (2.0%) in the uninstalled and installed cases, respectively. The discrepancy is larger in the uninstalled case because the propeller is operating in the non-linear region (low advance ratio) of the thrust curve [26], at which a larger portion of the blades have stalled in the isolated configuration than in the installed configuration. Hence, the numerical model captures the performance of the installed propeller measurement more accurately, due to less flow separation on the blades. The onset of blade stall at these high-thrust conditions also implies that the thrust coefficient varies only slightly with advance ratio, which explains why the differences in thrust between the installed and uninstalled cases are relatively small ($\Delta C_T = 0.005$) when compared to the reductions in propeller thrust that are typically obtained in over-the-wing configurations [14, 19, 26].

Table 3 Pressure-lift and -drag coefficients, and thrust coefficients from the experimental (Exp.) and numerical (CFD) results.

	$c_{l,p}$	$c_{d,p}$	C_T
Exp. (uninstalled)	0.097	0.0111	0.353
Exp. (installed)	0.110	0.0089	0.348
CFD (uninstalled)	0.101	0.0080	0.336
CFD (installed)	0.167	0.0051	0.341

Table 4 Difference in coefficients between installed (inst.) and uninstalled (uninst.), as well as numerical and experimental results.

	$\Delta c_{l,p}$	$\Delta c_{d,p}$	ΔC_T
CFD vs. exp. (uninst.)	0.004	-0.0031	-0.017
CFD vs. exp. (inst.)	0.052	-0.0038	-0.007
Inst. vs. uninst. (exp.)	0.013	-0.0022	-0.005
Inst. vs. uninst. (CFD)	0.066	-0.0029	0.005

The computed lift-coefficient in the uninstalled case compares reasonably well with the measured one. The uninstalled drag coefficient from CFD, however, is $\Delta c_{d,p} = -0.0031$ lower than in the experiment, which represents a reduction of approximately 28%. This is attributed to the higher pressures obtained over the flap, as reflected in Fig. 10a. When the propeller is installed, the more pronounced propeller-induced flow separation of the experimental results leads to a lower circulation than in the numerical results. Consequently, the lift coefficient is $\Delta c_{l,p} = 0.052$ (45%) higher in the numerical approach. Analogously, the difference in drag between numerical and experimental results increases to $\Delta c_{d,p} = -0.0038$ (-43%) in the installed case, since lower pressures are obtained near the trailing edge in the experiment as a consequence of the increased flow separation. Hence, the lift enhancement and drag reduction due to the propeller installation is more pronounced in the numerical results than in the measurements. However, when comparing the resulting changes in lift, drag, and thrust due to the propeller installment, one can see that only the change in lift differs significantly between the numerical and experimental results, whereas the changes in drag and thrust are comparable. Furthermore, the the overall trend of lift increase and drag decrease due the propeller installment is captured by the numerical results.

This comparison shows that the results should be interpreted with caution and that no quantitative conclusions should be drawn based on the numerical results. Additionally, it should be noted that the relatively high percentage differences between experimental and numerical data is largely a consequence of the low reference lift and drag coefficients. Nevertheless, the objective of this study is to understand the interaction effects between an OTW propeller and the wing in a baseline and inclined configuration. By analyzing the results qualitatively, and keeping the aforementioned limitations in mind, the numerical evaluation of the problem can provide valuable insight into the different interaction mechanisms that govern the performance of the system.

IV. Aerodynamic Interaction Phenomena

This section describes the aerodynamic interaction phenomena between the wing and propeller for the baseline (Sec. IV.A) and inclined (Sec. IV.B) configurations. In particular, the discussion focuses on the velocities and pressures induced by the propeller, and their influence on flow separation over the flap. The reader is reminded that the following results are obtained without wind tunnel walls to remove their influence on the aerodynamic interaction.

A. Baseline configuration

In general, the wing geometry induces a vertical component of velocity in the plane of the propeller, that causes a downward deflection of the stream tube behind the propeller. Figure 12a shows the time-averaged axial velocity with streamlines in a vertical plane through the propeller axis. It can be seen that the change in vertical momentum over the flap is not large enough to re-direct the propeller slipstream completely. This results in an area of low axial velocity over the flap, similar to the flow in a divergent channel. The static pressure and in-plane velocity vectors induced by the propeller (i.e., the difference with respect to propeller-off conditions) are shown in Fig. 12b. The velocity vectors upstream of the propeller indicate that the upstream effect is weak. Only small decrease in the axial velocity U over the flap, in the range of $0.8 < x/c < 0.85$, is visible in Fig. 12b by the vector pointing opposite to the vectors inside the slipstream. This decrease in momentum is due to the divergence of the slipstream from the flap and slipstream contraction. Since the momentum decreases, the static pressure increases over the flap curvature and flow reversal occurs more upstream than without the propeller, as shown in Fig. 9.

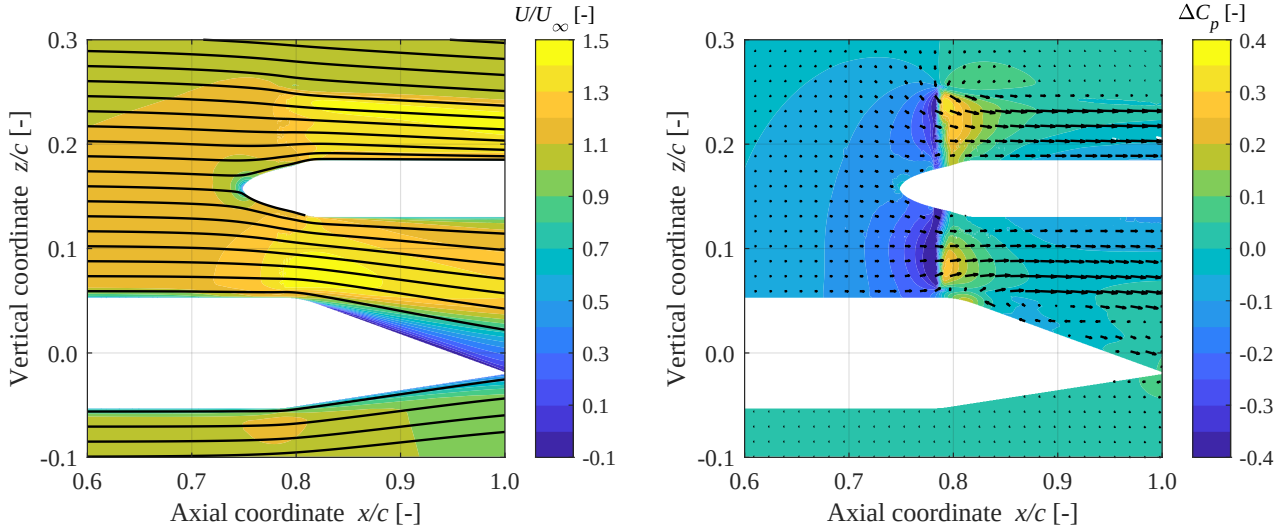

(a) Axial velocity. **(b) Induced Pressure and velocity.**

Fig. 12 Time-averaged axial velocity with streamlines (a) and induced pressure and velocities (b) at $y/c = 0$ for the baseline configuration.

The propeller-induced increase in static pressure over the flap curvature is also visible as a decrease of the suction peak in the pressure distribution of the wing profile below the propeller axis in Fig. 13. However, the pressure distribution is such that increased suction can be found upstream up the propeller and, consequently, the backward facing component of the suction peak is reduced. This is due to the upstream effect of the propeller, which not only increases the axial velocity along the center of the streamtube ($y/R = 0$) but also in the outboard areas ($y/R = \pm 0.77$), as shown in Fig. 14. Furthermore, additional leading edge suction can be achieved when the propeller is installed. Since the upstream effect of the propeller is relatively small, this enhanced leading edge suction is attributed to the overall increase in circulation of the wing. Hence, the propeller augments lift by increasing suction on the wing, and reduces drag, due to more pronounced leading edge suction and a reduced backward facing component of the suction peak.

A significant spread in the propeller-on pressure distribution can also be observed surrounding the suction peak. This represents the unsteady loads on the wing, caused by the propeller. To investigate to what extent these unsteady pressures affect the flow field, Fig. 15 presents the wall-shear lines and propeller-induced pressure distribution on the wing, in a time-averaged and time-accurate sense. This figure also includes spanwise vorticity contours in the $y/c = 0$

plane, indicating the position of the tip vortices. Figures 15a to 15c show that the reduction in the pressure coefficient on the wing is significantly larger for a phase angle of zero degrees compared to, for instance, 30 degrees and the time-averaged result. It was observed that the low-pressure field of the blade's suction side merges with the low-pressure field of the wing's suction side, increasing the suction on the wing, when a propeller blade is close to the wing surface. This explains why the lift of a wing increases the most when the tip clearance between the wing an OTW propeller is smallest, as observed in earlier studies [12, 13, 38], assuming that no severe flow separation occurs behind the propeller.

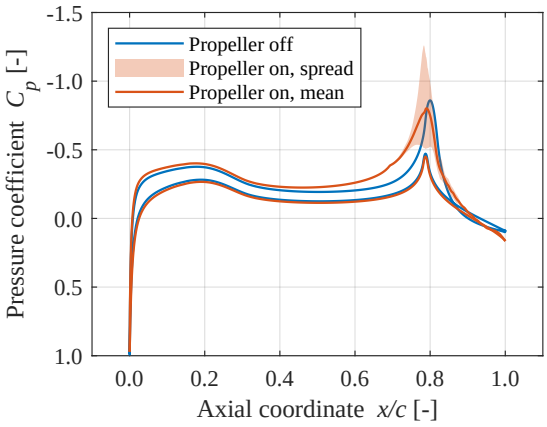

Fig. 13 Pressure distribution of the wing profile at y/c=0 in the baseline configuration.

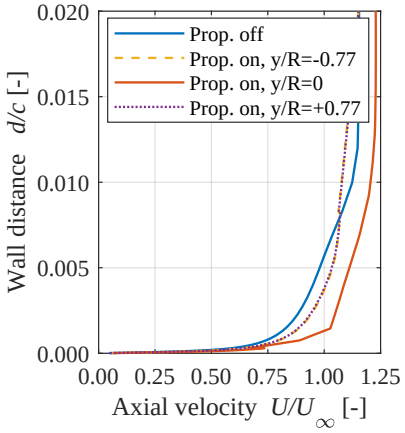

Fig. 14 Boundary-layer profiles 0.5R ahead of the propeller, at three spanwise locations.

The time-averaged shear-lines in Fig. 15a show that flow reversal is centered directly below the propeller axis. This is mainly attributed to the mass flow deficit in the region between the flap wall and the edge of the propeller-slipstream diverging from it. Previous research [24] shows that the intensity of flow reversal below the propeller axis increases with propeller thrust and the phenomena itself cannot be mitigated effectively by increasing the propeller clearance. Away from the propeller axis, the lobes visible along the separation line in Fig. 15a show that flow separation has locally been postponed. This is due to the increased velocity upstream of the propeller, which increases the momentum in the boundary-layer of the wing, as reflected in Fig. 14. This in turn increases its capability to withstand the adverse pressure gradient over the flap.

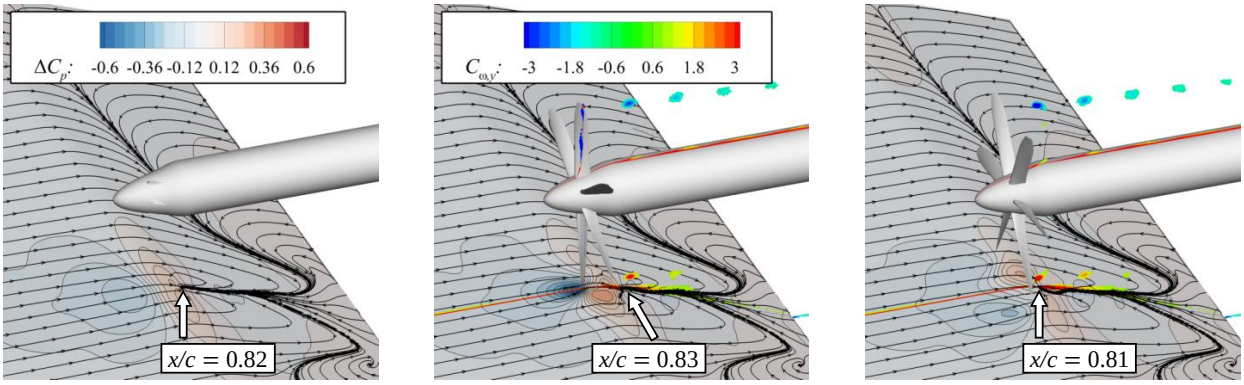

(a) Time-averaged. **(b) $\phi = 0°$.** **(c) $\phi = 30°$.**

Fig. 15 Time-averaged (a) and unsteady (b,c) influence of the propeller on the surface-pressure distribution and wall-shear lines of the wing, in the baseline configuration. Vorticity contours shown in $y/c = 0$ plane for $|C_{\omega,y}| > 1.5$.

The influence of the blade tip vortices can be inferred from the time-accurate results in Figs. 15b and 15c. The point of flow separation has a temporal dependency on the position of the blade tip vortices due to their momentary increase in adverse pressure gradient. The arrows in Figs. 15b and 15c indicate that the in-plane location of flow separation is

below the most upstream blade tip vortex at both phase angles. In both the time-averaged and unsteady flow fields, the point of flow separation is downstream of the propeller disk. Hence, instead of directly forcing flow separation, the adverse pressure gradient at the propeller location only weakens the boundary-layer. The remaining momentum is then not sufficient anymore to withstand the additional adverse pressure gradient of the flap and blade tip vortices downstream of the propeller. This effect is centered below the propeller since the propeller slipstream is closest to the wing there and, hence, the momentum deficit above the flap and the influence of the blade tip vortices is strongest.

B. Inclined configuration

Analogously to the baseline configuration, the flowfield induced by the inclined propeller is shown in Figs. 16a and 16b to explain the influence of the propeller on the pressure distribution of the wing. When the propeller is deflected together with the flap, not only the downwash of the wing geometry introduces a vertical velocity component in the slipstream, but also the inclination of the propeller directs the slipstream along the propeller axis. Figures 16a and 16b show that the momentum deficit over the flap is filled by the slipstream and the velocity over the flap is increased. Consequently, a stronger adverse pressure gradient, compared to the baseline configuration, can be tolerated. The additional momentum in the boundary-layer of the flap, due to propeller inclination is shown in Fig. 17, where the velocity u is the component of the axial velocity that is parallel to the flap-surface. From both Fig. 16a and Fig. 16b it can also be inferred that the propeller thrust and, therewith, the maximum in induced velocity and minimum in induced pressure, is shifted towards the upper half of the propeller disk, away from the wing. Thus, the suction on the wing, in front of the propeller, is less enhanced than in the baseline case.

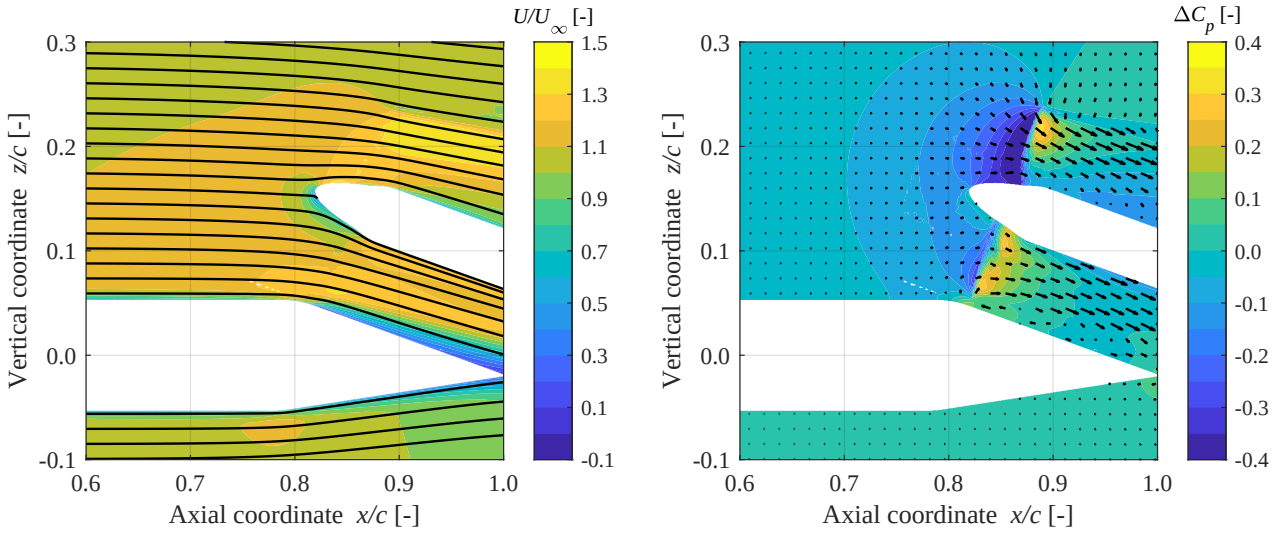

(a) Axial velocity. **(b) Induced pressure and velocities.**

Fig. 16 Time-averaged axial velocity with streamlines (a) and induced pressure and velocities (b) at $y/c = 0$ for the inclined configuration.

The influence of the inclined propeller on the wing pressure distribution is shown in Fig. 18. The main difference with respect to the baseline pressure distribution is that the pressure reduction in front of the propeller is smaller in the inclined case. Moreover, while the suction peak over the flap is reduced in the baseline configuration due to increased flow separation, in the baseline configuration the pressure peak over the flap is maintained.

In Fig. 19, the wall-shear lines and propeller-induced pressure distribution on the wing are shown again for the inclined-propeller configuration. It can be seen that the propeller locally triggers flow separation, directly beneath the propeller disk, since the propeller is now behind the hinge line and the adverse pressure gradient generated by the propeller is superimposed to the pressure gradient on the flap. However, contrary to the reversed flow over the entire flap chord in the middle of the baseline configuration, this separation is followed by an immediate reattachment of the flow. This reattachment occurs because, in this configuration, the high-momentum flow in the slipstream is parallel to the flap surface, as discussed in Ref. [24].

The wall-shear lines provided in Fig. 19 show that, by inclining the propeller, momentum is added to the boundary-layer of the wing, that ultimately prevents flow separation. Moreover, while in the baseline configuration flow separation on the flap was only postponed below the outboard part of the slipstream, the results of the inclined propeller indicate the possibility of completely attached flow in those regions. Since the propeller already induces vertical momentum, less suction is necessary on the surface of the wing to deflect the flow downwards. Therefore, the boundary-layer can withstand the pressure gradients on the flap. The time-dependent results in Figs. 19b and 19c show that the blade tip vortices merely vary the chordwise extent of the local flow separation beneath the propeller. However, the overall flow field exhibits no significant dependency on the blade phase angle.

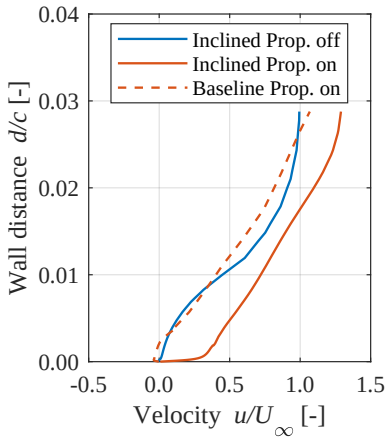

Fig. 17 Time-averaged velocity profile over the flap at $x/c = 0.9$, below the propeller axis.

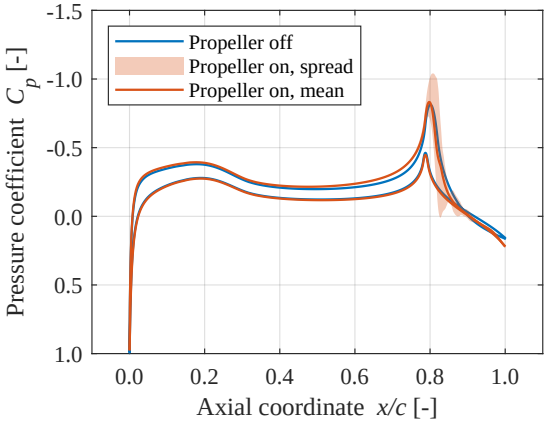

Fig. 18 Pressure distribution of the wing profile at $y/c = 0$ in the inclined configuration.

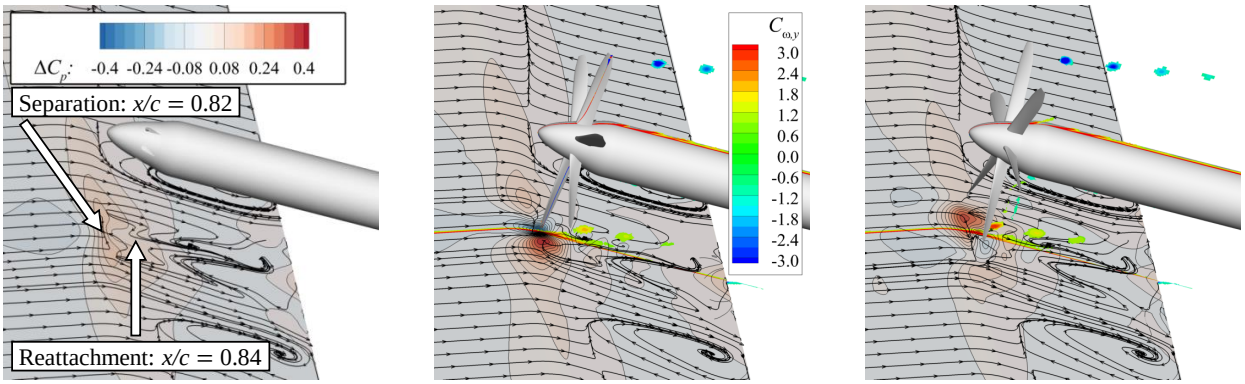

(a) Time-averaged. **(b) $\phi = 0°$.** **(c) $\phi = 30°$.**

Fig. 19 Time-averaged (a) and unsteady (b,c) influence of the propeller on the surface-pressure distribution and wall-shear lines of the wing, in the baseline configuration. Vorticity contours shown in $y/c = 0$ plane for $|C_{\omega,y}| > 1.5$.

V. Effect on Wing and Propeller Loads

After having analyzed the aerodynamic interaction effects for both configurations in the previous section, this section describes how the aerodynamic interaction influences the distribution of forces generated by the propeller and wing. First, the propeller loading distributions will be compared between the baseline and inclined configuration in Section V.A. Then, the spanwise distributions of lift and drag of the wing are compared for the two configurations.

A. Propeller loading distributions

The wing induced flowfield results in a modified propeller loading and propeller thrust. Compared to the isolated thrust coefficient of $C_T = 0.336$, the baseline propeller thrust increases by $\Delta C_T = 0.005$, which is less than 2 % of the isolated thrust. The small increase obtained in this configuration can be explained by analyzing the thrust distribution on the propeller disk, shown in Fig. 20a. The wing induces a flowfield to the propeller such that there is higher axial velocity, as well as a vertical velocity component. The vertical component results in a net negative angle of the inflow to the propeller disk and, hence, a strong increase and moderate decrease of the blade angle of attack for the up-going and down-going blades, respectively. This causes the asymmetry in the thrust distribution in Fig. 20a. A higher axial velocity typically reduces the blade angle of attack and, therewith, the thrust, over the entire propeller disk. However, due to the low lift coefficient of the wing, this effect is small compared to the angle of attack effect. A similar asymmetry in the thrust distribution of a propeller close to the trailing edge of a wing and at a low lift coefficient, caused by vertically wing-induced velocities, was also predicted with a BEM code and confirmed by experimental measurements in a previous study [19].

In the inclined configuration (Fig. 20b), the propeller inclination is larger than the local flow angle induced by the wing. Therefore, the inclined propeller disk experiences a net positive angle of attack to the inflow, and the in-plane velocities increase the blade angle of attack for the down-going blades, contrary to the baseline case. The local thrust increase for the inclined propeller is larger in magnitude than for the baseline propeller, but confined to a smaller area on the disk. Consequently, the thrust coefficient, $C_T = 0.335$, of the inclined propeller is lower than that of the baseline propeller, but comparable to the isolated propeller thrust. Close to the wing, the thrust augmentation fades as the inflow is more aligned with the propeller axis again and the axial velocity increases. Compared to the baseline configuration, the inclined propeller produces less thrust close to the wing. Hence, there are smaller induced velocities and the tip vortices are weaker. The smaller induced velocities and the up-tilt of the propeller-induced pressure field, explain why the upstream reduction of pressure on the wing is less pronounced in the inclined configuration than in the baseline configuration. Weaker blade tip vortices, on the other hand, cause smaller additional adverse pressure gradients on the flap.

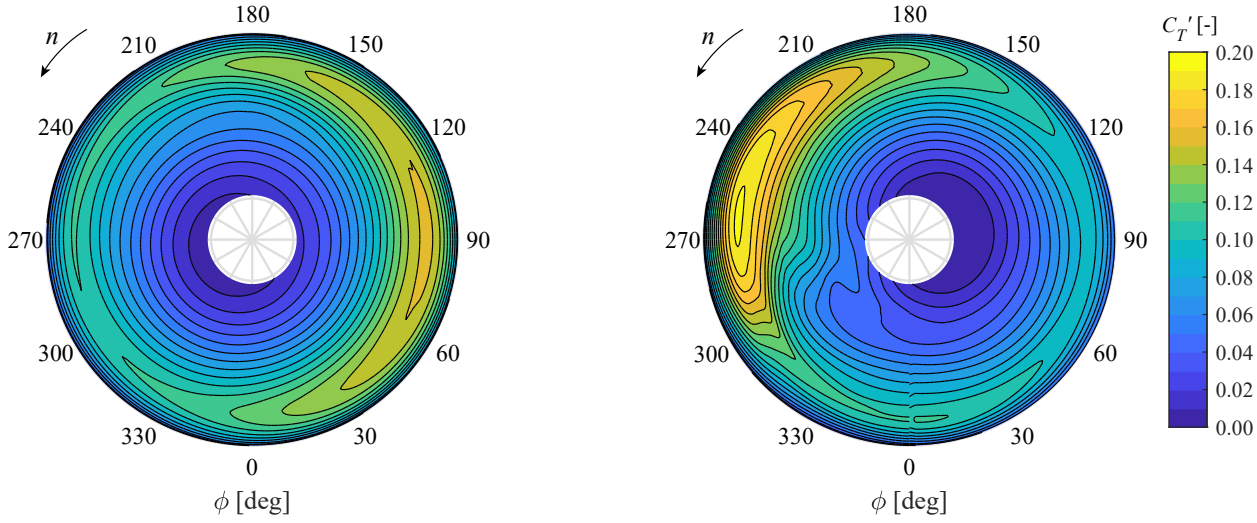

(a) Baseline. **(b) Inclined.**

Fig. 20 Thrust distribution on the propeller disk.

Although the total thrust along the propeller axis exhibits only a small change when the propeller is inclined, the force in flight direction, F_x, changes considerably. The propeller-fixed coordinate system with the thrust along the propeller axis and a normal force N perpendicular to it is sketched in Fig. 21. It should be noted that F_x is sketched in the negative x-direction and, thus, is negative. The resultant force R has a reduced component in x-direction because it needs to compensate for the backward component of the normal force. It becomes obvious that when the propeller is inclined, not only the horizontal force F_x decreases, but also the vertical force F_z increases, due to the thrust vectoring. A comparison of the individual time-averaged force components is given in Table 5. The $\hat{T}_c$ coefficients in table 5 are

normalized with the reference area $S_{\text{ref}} = 1.1cD_{\text{p}}$ to be comparable to the lift and drag coefficients of a wing segment of $1.1D_{\text{p}}$ span for a distributed propeller application, where multiple propellers would be installed in close proximity—for example, with a hypothetical tip clearance of $0.1D_{\text{p}}$. The subscripts N, x, z and R indicate which force component is taken. The results in Table 5 confirm that the thrust in the flight direction, $\hat{T}_{c,x}$, decreases, while the vertical component, $\hat{T}_{c,z}$, increases when the propeller is inclined. The vertical component becomes more pronounced for two reasons: firstly, because the thrust vector is tilted upwards, and secondly, because the normal force on the propeller is stronger due to the angle-of-attack effect.

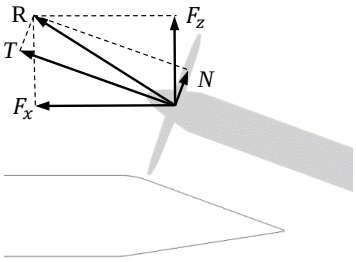

Fig. 21 Sketch of the forces acting on the inclined propeller. The vectors are not to scale.

Table 5 Comparison of the time-averaged forces for the different propeller installations.

Parameter	Baseline	Inclined	Isolated
$\hat{T}_c$	0.094	0.093	0.093
$\hat{T}_{c,N}$	-0.009	0.022	0
$\hat{T}_{c,x}$	-0.094	-0.080	-0.093
$\hat{T}_{c,z}$	-0.009	0.053	0
$\hat{T}_{c,R}$	0.095	0.096	0.093
C_T	0.341	0.335	0.336

The torque and shaft power of the inclined propeller ($C_Q = 0.1029$, $C_P = 0.647$) change only slightly compared to both the baseline results ($C_Q = 0.1022$, $C_P = 0.642$) and the isolated values ($C_Q = 0.1023$, $C_P = 0.643$). In fact, the change in torque coefficient falls within the uncertainty determined in Sec. III.A. Since the shaft power required in the two configurations is comparable, the results of Table 5 indicate that the propeller efficiency is highest in the baseline configuration, if only the thrust in the direction of flight is considered.

B. Wing loading distributions

The propeller induces velocities that affect not only the pressure distribution of the wing at the propeller location, but also the distribution of lift and drag along the span. The time-averaged spanwise lift and drag distribution of the wing are shown in Fig. 22. As a reference, the same coefficients are also given for the isolated wing and the wing with nacelle, excluding the propeller blades. In the baseline configuration, the locally induced suction by the propeller results in a peak of the lift in the middle of the wing, below the propeller axis. Contrary to the centered lift peak, the lowest drag is shifted below the outboard part of the up-going blade. This is due to a higher blade loading on the up-going blade side, which increases the static pressure behind the propeller disk and consequently reduces the pressure drag. Below the down-going blade, the drag saved by the propeller merely compensates for the additional drag of the nacelle resulting in a propeller-on drag coefficient close to the one of the isolated wing.

Despite the delay of flow reversal on the flap, the lift distribution in the inclined configuration exhibits a smaller rise in lift coefficient than the baseline configuration, due to the relatively weak induced velocities close to the wing. The drag, however, shows a larger reduction, which is associated to the postponement of flow separation on the flap. Moreover, axial vorticity distributions in the wake (not shown here) indicate that the relative effect of trailing vorticity due to the non-uniform spanwise loading on the induced angle of attack is negligible. Hence, the inclined configuration presents larger drag reductions than the baseline case, while the baseline configuration shows a larger lift increase.

To evaluate the system forces in a hypothetical distributed-propulsion application where the tip clearance between adjacent propellers is 10% of the propeller diameter, the differences between the propeller on and propeller off lift and drag distributions are integrated over a wing segment of $1.1D_{\text{p}}$ span. Since the resulting force coefficients, ΔC_L and ΔC_D, represent the change in lift and drag of a wing segment due to the propeller, they can be added to the lift and drag coefficients of the isolated wing segment, plus the thrust coefficients of the propeller in the respective direction (from Table 5) to obtain the total forces for an OTW propeller system. It should be noted, however, that this procedure does not account for interaction effects that would be present with multiple adjacent propellers. This leads to conservative results, since the propeller also increases lift and decreases drag beyond the $1.1D_{\text{p}}$ interval, as reflected in Fig. 22. This contribution would be superimposed to the changes in lift and drag created by the adjacent propeller on the adjacent wing section, and vice versa. Table 6 shows that the additional vertical force component of the propeller in the inclined configuration compensates for the weaker lift increase of the wing segment (ΔC_L), such that the total force

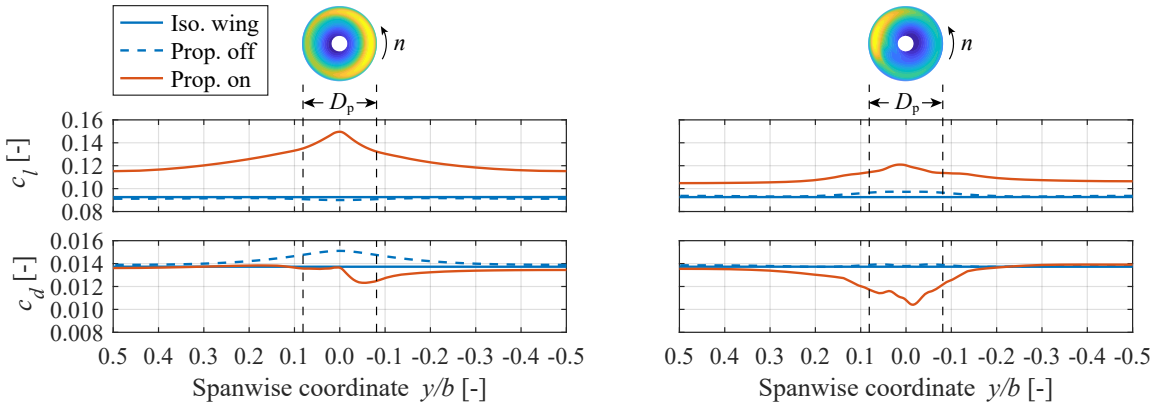

(a) Baseline configuration. **(b) Inclined configuration.**

Fig. 22 Sectional lift (top) and drag (bottom) coefficient distributions along the wingspan in the baseline (a) and inclined (b) configurations.

in the vertical direction is 24% larger than for the baseline propeller configuration. This effective lift increase due to propeller inclination can be even higher in terms of the maximum attainable lift coefficient, since the postponed flow separation over the flap is likely to shift the maximum lift coefficient to higher angles of attack. The inclination of the propeller, however, also leads to a weaker additional forward force, $\hat{T}_{c,x}$, to the system. This reduction in net thrust is not compensated by the decrease in drag of the wing (ΔC_D), as can be inferred from Table 7. Hence, the baseline configuration has a 20% larger installed thrust than the inclined configuration. Interestingly, due to the comparable thrust in the x-direction for the baseline and isolated configuration, the drag saved on the baseline wing also leads to a larger installed thrust compared to the isolated configuration. Since the shaft power coefficient is comparable in the two cases, this confirms that an OTW propulsion system can present an increased aero-propulsive efficiency compared to a decoupled system.

Table 6 Balance of forces in z-direction for a wing-segment span of $b'/D_p = 1.1$, at the same shaft power.

Configuration	C_L^{iso} [-]	ΔC_L [-]	$\hat{T}_{c,z}$ [-]	Total
Isolated	0.093	0	0	0.093
Baseline	0.093	0.050	-0.009	0.134
Inclined	0.093	0.020	0.053	0.166

Table 7 Balance of forces in x-direction for a wing-segment span of $b'/D_p = 1.1$, at the same shaft power.

Configuration	C_D^{iso} [-]	ΔC_D [-]	$\hat{T}_{c,x}$ [-]	Total
Isolated	0.0137	0	-0.093	-0.0793
Baseline	0.0137	-0.0018	-0.094	-0.0821
Inclined	0.0137	-0.0025	-0.080	-0.0688

VI. Conclusions and Recommendations

In this paper, the aerodynamic interaction between a wing and a tiltable OTW propeller has been studied by performing unsteady RANS simulations. A comparison to experimental data shows that the CFD simulations can predict propeller thrust and lift of the isolated wing accurately. However, a comparison of the installed configuration shows that the magnitude of propeller-induced flow separation is under-predicted in the numerical approach. The discrepancy is caused by the influence of the overset interface on flow gradients in the boundary-layer, the modeling of turbulence used by the RANS solver, and an under-estimation of tip-vortex strength due to numerical diffusion and dissipation. Therefore, although the selected numerical approach captures the phenomena and trends observed in earlier experimental studies, predicting the exact location and magnitude of flow separation in OTW systems with unsteady RANS simulations remains a challenge.

The results of the baseline configuration show that the propeller generates a low-pressure region on the wing surface upstream of the propeller disk. Directly behind the propeller, the pressure on the wing surface is higher, due to the static pressure increase accross the propeller disk and the divergence of the slipstream from the flap surface. The simulations

suggest that the resulting adverse pressure gradient does not immediately cause flow separation at the propeller location, but only weakens the boundary-layer. The flow over the flap separates further downstream, due to the continued adverse pressure gradient and the periodic momentum deficits induced in the boundary-layer by the tip vortices. However, this phenomena is dominant only below the propeller axis, where the slipstream, and also the blade tip vortices, are closest to the wing. Moreover, the location of flow separation is found to vary only slightly throughout a blade passage, despite the unsteady excitation by the tip vortices.

The inclined propeller creates less suction on the wing, since the combination of propeller inclination and wing-induced inflow lead to a reduced thrust production close to the wing surface. In this configuration, the flow separates locally beneath the propeller and is subsequently reattached due to the high-momentum slipstream which flows parallel to the flap surface. However, despite the postponed flow separation, the inclined case does not to enhance the lift over the flap when compared to the baseline case at the same angle of attack, because of the higher static pressure in the propeller slipstream. The higher static pressure does, however, decrease the pressure drag of the wing when compared to the baseline case.

The presence of the wing significantly alters the loading distribution on the propeller disk. However, the overall thrust generated in the direction of the propeller axis is not significantly affected by the wing, for both configurations. In the inclined configuration, the additional vertical force component of the propeller compensates for the weak lift augmentation of the wing segment below the propeller diameter. This results in a larger lift of the inclined OTW propeller–wing system compared to the baseline system. However, the inclination of the propeller leads to a weaker forward-facing force component. This reduction in net thrust is not compensated by the drag saved on the wing. Hence, the inclined configuration creates more lift than the baseline configuration, at the cost of less installed forward thrust.

The findings of this study confirm the high-lift potential of tiltable, distributed OTW propeller systems, contributing towards the development of novel aircraft configurations with improved propulsion-system integration. However, several aspects of the numerical setup can be improved, and directions for future research can be established. The overset interface was found to contribute to an inaccurate prediction of flow separation due to the interpolation of flow gradient. Thus, it should be avoided to place an overset interface in a region where high flow gradients are expected, like in a boundary-layer or within the area of influence of vortices. For an OTW propeller application, however, this is nearly impossible. Hence, a control simulation featuring an empty overset mesh should ideally be performed for every configuration that includes an overset interface to verify the results. Moreover, the mesh refinement plays a crucial role for an accurate prediction of the influence of the blade tip vortices. That being said, higher-fidelity simulations like LES are necessary to verify whether it is possible to numerically capture propeller-induced flow separation accurately. Furthermore, the comparison to the wind tunnel measurements highlighted the importance of having experimental data for validation to asses the uncertainty in the numerical results. Therefore, experiments of an distributed, inclined system are required to validate the performance of such a system.

References

[1] Chèze, B., Gastineau, P., and Chevallier, J., "Forecasting world and regional aviation jet fuel demands to the mid-term (2025)," *Energy Policy*, Vol. 39, No. 9, 2011, pp. 5147–5158.

[2] Bonet, J. T., Schellenger, H. G., Rawdon, B. K., Elmer, K. R., and Wakayama, S. R., "Environmentally Responsible Aviation (ERA) Project - N + 2 Advanced Vehicle Concepts Study and Conceptual Design of Subscale Test Vehicle (STV): Final Report," NASA CR-2011-216519, 2011.

[3] Darecki, M., Edelstenne, C., Enders, T., Fernandez, E., Hartman, P., Herteman, J.-P., Kerkloh, M., King, I., Ky, P., Mathieu, M., et al., "Flightpath 2050: Europe's vision for aviation," European Commission Report of the High Level Group on Aviation Research, 2011.

[4] Sehra, A., and Whitlow, W., "Propulsion and power for 21st century aviation," *Progress in Aerospace Sciences*, Vol. 40, No. 4-5, 2004, pp. 199–235.

[5] Patterson, M., "Conceptual design of high-lift propeller systems for small electric aircraft," Ph.D. thesis, Georgia Institute of Technology, 2016.

[6] Wick, A., Hooker, J., and Zeune, C., "Integrated Aerodynamic Benefits of Distributed Propulsion," 53rd AIAA Aerospace Sciences Meeting, Kissimmee, FL, USA, January 5-9 2015.

[7] Patterson, M., Derlaga, J., and Borer, N., "High-lift Propeller System Configuration Selection for NASA's SCEPTOR Distributed Electric Propulsion Flight Demonstrator," 16th AIAA Aviation Technology, Integration, and Operations Conference, Washington D.C., USA, June 13-17 2016.

[8] Kim, H. D., "Distributed propulsion vehicles," 27th Congress of the International Council of the Aeronautical Sciences, Nice, France, September 19-24 2010.

[9] Stoll, A., Bevirt, J., Moore, M., Fredericks, W., and Borer, N., "Drag Reduction Through Distributed Electric Propulsion," 14th AIAA aviation technology, integration, and operations conference, Atlanta, GA, USA, June 16-20 2014.

[10] Ma, Y., Zhang, W., Zhang, Y., Zhang, X., and Zhong, Y., "Sizing Method and Sensitivity Analysis for Distributed Electric Propulsion Aircraft," *Journal of Aircraft*, 2020.

[11] de Vries, R., Hoogreef, M. F. M., and Vos, R., "Preliminary Sizing of a Hybrid-Electric Passenger Aircraft Featuring Over-the-Wing Distributed-Propulsion," AIAA Scitech 2019 Forum, San Diego, CA, USA, January 7-11 2019.

[12] Johnson Jr., J., and White, E., "Exploratory Low-Speed Wind-Tunnel Investigation of Advanced Commuter Configurations Including an Over-the-Wing Propeller Design," Aircraft Design, Systems and Technology Meeting, Fort Worth, TX, USA, October 17-19 1983.

[13] Cooper, R., McCann, W., and Chapleo, A., "Over wing propeller aerodynamics," *ICAS Proceedings*, Vol. 18, American Institute of Aeronautics and Astronautics, 1992, pp. 266–266.

[14] Müller, L., Heinze, W., Kožulović, D., Hepperle, M., and Radespiel, R., "Aerodynamic Installation Effects of an Over-the-Wing Propeller on a High-Lift Configuration," *Journal of Aircraft*, Vol. 51, No. 1, 2014, pp. 249–258.

[15] Müller, L., Kožulović, D., and Radespiel, R., "Aerodynamic performance of an over-the-wing propeller configuration at increasing Mach number," *CEAS Aeronautical Journal*, Vol. 5, No. 3, 2014, pp. 305–317.

[16] Delfs, J., Faßmann, B., Lippitz, N., Lummer, M., Mößner, M., Müller, L., Rurkowska, K., and Uphoff, S., "SFB 880: Aeroacoustic research for low noise take-off and landing," *CEAS Aeronautical Journal*, Vol. 5, No. 4, 2014, pp. 403–417.

[17] Custer, W. R., "Channel wing airplane," US Patent 2,514,478, July 11 1950.

[18] Pasamanick, J., "Langley Full-Scale-Tunnel Tests of the Custer Channel Wing Airplane," NACA Research Memorandum L53A09, Washington D.C., USA, April 7 1953.

[19] Marcus, E. A. P., de Vries, R., Raju Kulkarni, A., and Veldhuis, L. L. M., "Aerodynamic Investigation of an Over-the-Wing Propeller for Distributed Propulsion," 2018 AIAA Aerospace Sciences Meeting, Kissimmee, FL, USA, January 8-12 2018.

[20] Perry, A., Ansell, P., and Kerho, M., "Aero-Propulsive and Propulsor Cross-Coupling Effects on a Distributed Propulsion System," *Journal of Aircraft*, Vol. 55, No. 6, 2018, pp. 2414–2426.

[21] Hermetz J., D. C., Ridel M., "Distributed electric propulsion for small business aircraft a concept-plane for key-technologies investigations," 30th Congress of the International Council of the Aeronautical Sciences ICAS, Daejon, South Korea, September 2016.

[22] Bento, H. F. M., de Vries, R., and Veldhuis, L. L. M., "Aerodynamic Performance and Interaction Effects of Circular and Square Ducted Propellers," AIAA Scitech 2020 Forum, Orlando, FL, USA, January 6-10 2020.

[23] Müller, L., Kožulović, D., and Friedrichs, J., "Unsteady Flow Simulations of an Over-the-Wing Propeller Configuration," 50th AIAA/ASME/SAE/ASEE Joint Propulsion Conference, Cleveland, OH, USA, July 28-30 2014.

[24] de Vries, R., van Arnhem, N., Avallone, F., Ragni, D., Vos, R., Eitelberg, G., and Veldhuis, L., "Aerodynamic Interaction Between an Over-the-Wing Propeller and the Wing Boundary-Layer in Adverse Pressure Gradients," AIAA Aviation 2019 Forum, Dallas, TX, USA, June 17-21 2019.

[25] de Vries, R., Brown, M., and Vos, R., "Preliminary Sizing Method for Hybrid-Electric Distributed-Propulsion Aircraft," *Journal of Aircraft*, Vol. 56(6), 2019, pp. 2172–2188.

[26] van Arnhem, N., de Vries, R., Sinnige, T., Vos, R., Eitelberg, G., and Veldhuis, L., "Engineering Method to Estimate the Blade Loading of Propellers in Nonuniform Flow," *submitted to AIAA Journal (manuscript accepted)*, 2020.

[27] Spalart, P., and Rumsey, C., "Effective Inflow Conditions for Turbulence Models in Aerodynamic Calculations," *AIAA journal*, Vol. 45, No. 10, 2007, pp. 2544–2553.

[28] Caruelle, B., and Ducros, F., "Detached-Eddy Simulations of Attached and Detached Boundary Layers," *International Journal of Computational Fluid Dynamics*, Vol. 17, No. 6, 2003, pp. 433–451.

[29] Deck, S., "Zonal-Detached-Eddy Simulation of the Flow Around a High-Lift Configuration," *AIAA Journal*, Vol. 43, No. 11, 2005, pp. 2372–2384.

[30] Muscari, R., and di Mascio, A., "Detached Eddy Simulation of the flow behind an isolated propeller," Third International Symposium on Marine Propulsors, Lanceston, Tasmania, Australia, May 5-8 2013.

[31] Wallin, S., and Johansson, A., "An explicit algebraic Reynolds stress model for incompressible and compressible turbulent flows," *Journal of Fluid Mechanics*, Vol. 403, 2000, pp. 89–132.

[32] Rhie, C., and Chow, W., "Numerical study of the turbulent flow past an airfoil with trailing edge separation," *AIAA journal*, Vol. 21, No. 11, 1983, pp. 1525–1532.

[33] Ferziger, J., and Peric, M., *Computational Methods for Fluid Dynamics*, Springer Science & Business Media, 2002.

[34] Chan, W. M., Gomez, R., Rogers, S. E., and Buning, P., "Best Practices in Overset Grid Generation," 32nd AIAA Fluid Dynamics Conference and Exhibit, St. Louis, MO, USA, June 24-26 2002.

[35] Eça, L., and Hoekstra, M., "A procedure for the estimation of the numerical uncertainty of CFD calculations based on grid refinement studies," *Journal of Computational Physics*, Vol. 262, 2014, pp. 104–130.

[36] Stokkermans, T. C. A., van Arnhem, N., Sinnige, T., and Veldhuis, L., "Validation and Comparison of RANS Propeller Modeling Methods for Tip-Mounted Applications," *AIAA Journal*, Vol. 57, No. 2, 2019, pp. 566–580.

[37] Hariharan, N., "Rotary-Wing Wake Capturing: High-Order Schemes Toward Minimizing Numerical Vortex Dissipation," *Journal of aircraft*, Vol. 39, No. 5, 2002, pp. 822–829.

[38] Müller, L., Kožulović, D., Hepperle, M., and Radespiel, R., "The influence of the propeller position on the aerodynamics of a channel wing," *AIAA Journal*, Vol. 38, No. 5, 2012, pp. 784–792.